

MIT Open Access Articles

*All-Solid-State Lithium Battery Fitted with Polymer Electrolyte
Enhanced by Solid Plasticizer and Conductive Ceramic Filler*

The MIT Faculty has made this article openly available. **Please share**
how this access benefits you. Your story matters.

As Published: 10.1149/2.1371814JES

Publisher: The Electrochemical Society

Persistent URL: <https://hdl.handle.net/1721.1/135860>

Version: Final published version: final published article, as it appeared in a journal, conference proceedings, or other formally published context

Terms of Use: Article is made available in accordance with the publisher's policy and may be subject to US copyright law. Please refer to the publisher's site for terms of use.





All-Solid-State Lithium Battery Fitted with Polymer Electrolyte Enhanced by Solid Plasticizer and Conductive Ceramic Filler

Fei Chen,^{1,z} Wenping Zha,¹ Dunjie Yang,¹ Shiyu Cao,¹ Qiang Shen,¹ Lianmeng Zhang,¹ and Donald R. Sadoway²

¹State Key Lab of Advanced Technology for Materials Synthesis and Processing, Wuhan University of Technology, Wuhan 430070, People's Republic of China

²Department of Materials Science and Engineering, Massachusetts Institute of Technology, Cambridge, Massachusetts 02139-4307, USA

The scalable multifunctional solid electrolyte (MSE) composed of poly(ethylene oxide)-solid oxide lithium-ion conductor $\text{Li}_7\text{La}_3\text{Zr}_2\text{O}_{12}$ -succinonitrile (PEO_{18} -LiTFSI-LLZO-SN) is demonstrated as a promising candidate for high performance all-solid-state batteries. Among these electrolytes, PEO_{18} -LiTFSI-7.5%LLZO-10%SN presents a highest ionic conductivity of $1.19 \times 10^{-4} \text{ S} \cdot \text{cm}^{-1}$ at room temperature and a much higher Li^+ transference number. Moreover, this MSE has a good electrochemical stability of 5.5 V vs. Li/Li^+ , and exhibits excellent interfacial compatibility against lithium electrode. Owing to the improved interface contact and enhanced Li^+ transference, the MSE-based ASSLBs present outstanding cycling and rate performance at 60°C. Notably, the initial discharge capacity at 1 C is $130.2 \text{ mAh} \cdot \text{g}^{-1}$, and after 500 cycles 80.0% capacity is retained. The cell can be operated normally at lower temperatures (30°C and 45°C) while still delivering a relatively high specific capacity.
© 2018 The Electrochemical Society. [DOI: 10.1149/2.1371814jes]

Manuscript submitted August 29, 2018; revised manuscript received November 1, 2018. Published November 17, 2018.

Rechargeable lithium-ion batteries (LIBs) with high energy storage density are environmentally friendly and widely used in many fields.^{1,2} However, since these batteries use volatile and flammable liquid electrolytes there are safety issues such as poor thermal and chemical stability, potential for leakage of electrolyte, formation of lithium dendrites, and internal short circuits that remain unresolved.^{3,4} Compared to the traditional LIBs, all-solid-state lithium batteries (ASSLBs) replacing liquid electrolyte with solid electrolytes are designed to improve safety and to simplify battery architecture.⁵

Solid polymer electrolytes (SPEs) exhibit numerous advantages such as high energy density, light weight, mechanical flexibility, and high packing efficiency, which make SPEs preferred alternatives to liquid electrolytes and promising components in high-performance ASSLBs and other high-energy-density power sources.⁶ More recently, there has been ongoing research directed toward SPEs with high ionic conductivity, excellent mechanical behavior, good electrochemical stability to meet the application requirements of ASSLBs.⁷ To date, SPEs for ASSLBs have been based on poly(ethylene oxide) (PEO), poly(methyl methacrylate) (PMMA), and poly(vinylidene fluoride) (PVDF) to which are added various lithium salts.⁸ Among these SPEs, PEO-based polymer electrolytes are the most widely used and studied polymer electrolytes.⁹ However, PEO-based composites usually suffer from poor electrochemical stability and low conductivity (10^{-8} – $10^{-6} \text{ S} \cdot \text{cm}^{-1}$) caused by the high degree crystallization of polymer chains.¹⁰ Such inadequacies could be addressed by the design of novel PEO-based composites possessing a wider electrochemical window in conjunction with sufficient ionic transport properties.

The addition of plasticizers is considered to be an efficient solution to suppress the high degree of crystallization in a polymer. However, liquid plasticizers will greatly detract from the mechanical properties of polymer electrolytes; furthermore, the attendant flammability and volatility will give rise to problems in safety and stability.¹¹ These concerns prompted the development of a solid block copolymer electrolyte comprising blocks with sub-ambient glass transition temperatures, the blocks decorated with liquid-like brushes of PEO.¹² An alternative approach is to replace the liquid plasticizer with a solid plasticizer to maintain the safety and mechanical properties. Owing to its presence as a single plastic phase between -35°C to 62°C , succinonitrile (SN) has received much attention for its potential use in ASSLBs as a solid plasticizer.¹³ Because SN shows trans-gauche isomerism involving rotation of molecules about the central C–C bonds, electrolytes composed of lithium salts dissolved in SN exhibit exceptionally high ionic conductivity at room temperature.¹⁴ In addition,

the plasticity of SN can improve contact between the electrolyte and the electrodes.

Another strategy to improve transport properties and to enhance the mechanical strength of the SPEs is to incorporate ceramic fillers into a host PEO matrix. Many different oxides have been studied, including the classical TiO_2 ¹⁵ and SiO_2 ¹⁶ as well as the Li^+ -conductive $\text{Li}_{1.3}\text{Al}_{0.3}\text{Ti}_{1.7}(\text{PO}_4)_3$ ¹⁷ and $\text{Li}_{10}\text{GeP}_2\text{S}_{12}$.¹⁸ The addition of filler to the PEO promotes glass formation and inhibits crystallization¹⁹ which in turn improves the ionic conductivity of the polymer electrolyte, its mechanical properties, and its ability to make good electrical contact with the electrode. However, in previous reports^{20–22} at high filler content the improvements in ionic conductivity ($>10^{-4} \text{ S} \cdot \text{cm}^{-1}$) are realized mainly at high temperatures.

Recently, the garnet-structured, solid-oxide, lithium-ion conductor $\text{Li}_7\text{La}_3\text{Zr}_2\text{O}_{12}$ (LLZO)^{23–27} has been extensively studied as solid electrolyte for ASSLBs for its high Li^+ conductivity (10^{-4} – $10^{-3} \text{ S} \cdot \text{cm}^{-1}$), good thermal stability, interfacial compatibility against lithium metal, and wide electrochemical window ($\sim 6 \text{ V}$ vs. Li/Li^+). Since the interfacial resistance between the electrodes and pellet-type ion conductors is difficult to manage and ceramics are fragile and brittle, it is more difficult to achieve large-scale production and use of ceramic-based electrolytes than with polymer-based electrolytes. To the best of our knowledge, although SN and LLZO have multifunctional advantages as aforementioned, there have been no reports of combined addition of SN and a garnet-type ion conductor to a PEO-based solid electrolyte for ASSLB applications.

Herein, a scalable multifunctional solid electrolyte (MSE) was designed and synthesized by incorporating low concentrations of SN and Al-substituted LLZO into PEO. The plasticity of solid plasticizer SN could be an effective solution to the interface contact problems between electrodes and electrolyte, while active filler LLZO could help to improve the electrochemical window and mechanical strength of the composite electrolytes.²⁰ In addition, both SN and LLZO greatly improve ionic transport properties because LLZO and SN particles have positive effects on increasing free lithium ion concentrations and suppressing PEO crystallization.^{28,29} The synergetic effects of SN and LLZO on phase behavior, transport properties, and electrochemical stability of the MSE membranes were systematically assessed. Finally, the cycling and rate performance of ASSLBs based on these novel MSEs were investigated.

Experimental

Fabrication of the MSE membranes.—All experiments were carried out in glove boxes under argon atmosphere to avoid the effects

^zE-mail: chenfei027@whut.edu.cn

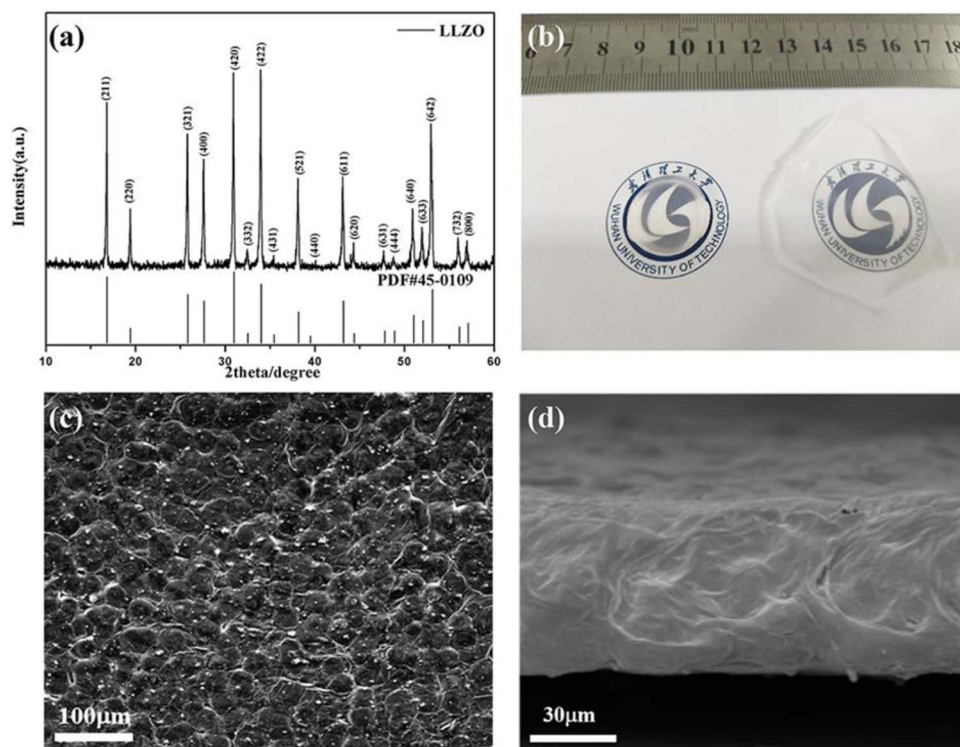


Figure 1. a) Comparison of XRD patterns of LLZO powder and the standard cubic $\text{Li}_7\text{La}_3\text{Zr}_2\text{O}_{12}$ (PDF#45-0109), b) photograph, c) SEM image, and d) cross-sectional SEM image of the MSE membrane (PEO_{18} -LiTFSI-7.5%LLZO-10%SN).

of water and oxygen on the raw materials (H_2O and $\text{O}_2 < 0.1$ ppm). The LLZO with 1.5 wt% $\gamma\text{-Al}_2\text{O}_3$ as additive was prepared at 1100°C using field assisted sintering technology (FAST). The preparation and sintering procedure of LLZO is based on a previous report in our laboratory.³⁰ Then the ceramic pellet was ground into powder, and the size of powder was controlled by planetary ballmilling and sieving with 500-mesh sieves. The size of LLZO particles was controlled within $1\ \mu\text{m}$ by planetary ballmilling and sieving with 500-mesh sieves. The PEO_{18} -LiTFSI-xLLZO-ySN electrolyte containing x wt% LLZO and y wt% SN (99%, Aladdin) was fabricated via conventional solution-casting technique, wherein the molar ratio of PEO ($M_w = 5 \times 10^6$, Aladdin) and LiTFSI (99%, Aladdin) is 18:1. The homogeneous slurry was formed after stirring LLZO, PEO, LiTFSI, and SN in acetonitrile (ACN, Aldrich) in glove boxes under argon atmosphere. The electrolyte membrane was obtained by wet coating the final slurry on a Teflon plate with a doctor blade and dried at 45°C in a vacuum oven for 24h to evaporate the acetonitrile.

Characterization of the MSE membranes.—The crystal structures of various samples were examined by X-ray diffraction (XRD, Rigaku Ultima III) measurements in the range of $10^\circ \sim 60^\circ$. Field-emission scanning electron microscopy (FEI-Quanta-250) was used to observe the morphologies of LLZO powder and MSE membranes. Differential scanning calorimetry (DSC, PYRIS1DSC) measurements were performed from -60°C to 90°C with a heating rate of $10^\circ\text{C min}^{-1}$ to observe the phase transition behavior of each solid electrolyte.

An electrochemical work station (CHI660E) was used to investigate various electrochemical measurements of the solid electrolyte. The ionic conductivity from 25°C to 75°C was obtained by the electrochemical impedance spectroscopy (EIS) in the frequency range of $1\ \text{MHz} \sim 10\ \text{Hz}$ using a SS/electrolyte/SS (stainless steel) block cell. In order to achieve thermal equilibrium, each test temperature will be kept for one hour before impedance measurements. SS/electrolyte/Li cells were fabricated to perform the linear sweep voltammetry (LSV) experiments within the test range of 2.5 V to 6 V (vs. Li^+/Li). The ion transference number (t_{Li^+}) was obtained by measurements of AC

impedance and DC polarization (with a polarization potential (ΔV) of 10 mV) at 60°C using symmetric Li/electrolyte/Li cells. The t_{Li^+} was calculated as

$$t_{\text{Li}^+} = \frac{I_{\text{ss}} (\Delta V - I_0 R_0)}{I_0 (\Delta V - I_{\text{ss}} R_{\text{ss}})} \quad [1]$$

where I_0 and I_{ss} present the initial and steady polarization currents, R_0 and R_{ss} present the initial and steady interfacial resistances. The interfacial stability against lithium electrode for different aging time was measured by EIS at 60°C using a Li symmetric cell.

Assembly and electrochemical performance of ASSLBs.—CR2025-type batteries consisted of LiFePO_4 and lithium pellet as the cathode active material and the anode were assembled in an Ar-filled glove box. The cathodes were prepared by mixing LiFePO_4 or LiCoO_2 , Super-P, PEO-LiTFSI (molar ratio EO: Li = 18:1) and SN, and the weight ratio of them is 7:1:1.5:0.5. The charge and discharge tests of the ASSLBs were carried out using a battery test instrument (CT2001A, LANHE). The active materials loading is $3.5 \sim 4.0\ \text{mg} \cdot \text{cm}^{-2}$.

Results and Discussion

Characteristics of MSEs.—LLZO was prepared by FAST in which the synthesis of high-purity cubic LLZO was accomplished in a one-step sintering process.³⁰ As presented in Fig. 1a, the XRD patterns of LLZO powder after ballmilling matched well the standard pattern of cubic $\text{Li}_7\text{La}_3\text{Zr}_2\text{O}_{12}$ (PDF#45-0109), and the SEM image (Fig. S1) indicates that the LLZO powder is fine and evenly distributed. As shown in Fig. 1b, the addition of LLZO powder makes the MSE membrane semi-transparent. In Fig. 1c, SEM image of the MSE membrane shows that the surface of the membrane consists of a series of visible folds and that the LLZO powder is well embedded into the polymer without obvious agglomeration. The cross-sectional image of the MSE membrane depicted in Fig. 1d shows the thickness to be about $60\ \mu\text{m}$.

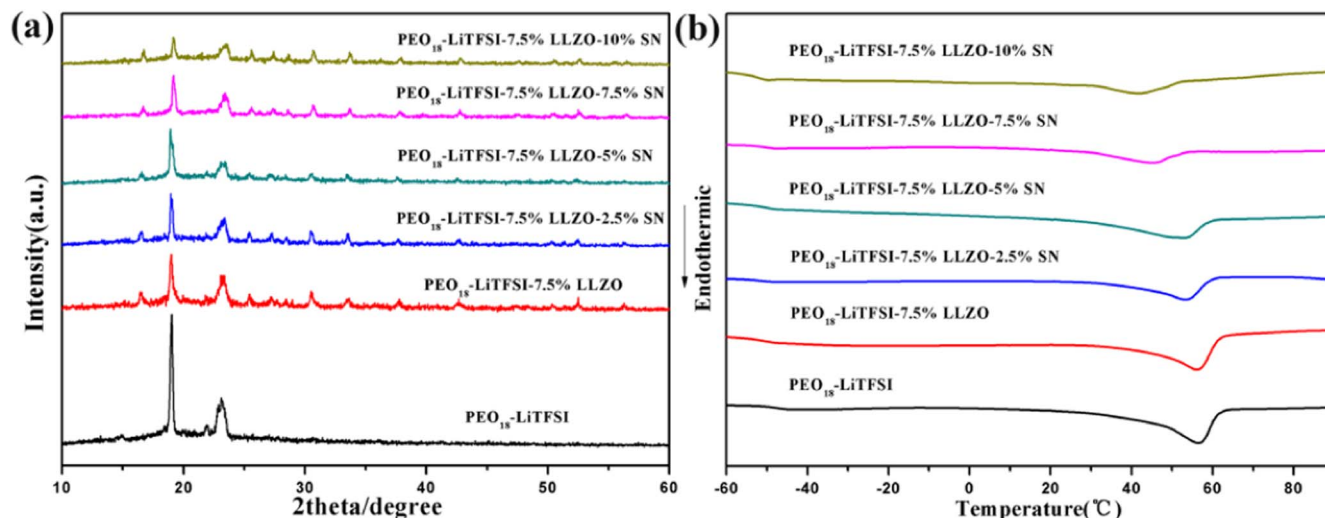


Figure 2. Variation with composition: a) X-ray diffraction and b) differential scanning calorimetry.

PEO is a widely used semi-crystalline polymer electrolyte; however, the crystallization of PEO will greatly affect ion migration and phase transition behavior. In Fig. 2a, XRD patterns of PEO₁₈-LiTFSI and MSEs with different SN contents are shown. PEO₁₈-LiTFSI electrolyte presents two broad characteristic diffraction peaks at $2\theta = 19^\circ$ and 23° .³¹ After incorporating LLZO and SN particles, the intensities of the crystalline peaks in PEO were significantly reduced, and further decreased as the SN content increases. The increase in the amorphous phase can be attributed to the physical interaction between SN, LLZO, and PEO, which destroys the ordered arrangement of polymer segments.^{22,32} The content of SN was limited to less than 10 wt% to render the thin film self-standing.

Fig. 2b shows the thermograms taken over the temperature range from -60°C to 90°C . The DSC thermograms reveal that the addition of LLZO and SN particles to PEO₁₈-LiTFSI electrolyte decreases the values of both T_g and T_m , resulting in lower crystallinity. The measured values of glass transition temperature (T_g), glass transition temperature (T_g), and the corresponding enthalpy of fusion (ΔH_m) from DSC are summarized in Table I. The relationship between relative degree of crystallinity (χ_c) and composition is given by

$$\Delta\chi_c = \frac{\Delta H_m}{\Delta H_{PEO}} \times 100\% \quad [2]$$

where ΔH_{PEO} is the enthalpy of fusion of 100% crystalline PEO, $\Delta H_{PEO} \approx 203 \text{ J} \cdot \text{g}^{-1}$.^{33,34} The T_g of the PEO₁₈-LiTFSI electrolyte decreased from -48.21°C to -49.95°C by incorporation of 7.5% LLZO and further decreased to the lowest temperature of -52.73°C thanks to the addition of 10% SN. The decrease in T_g should be accompanied by an increase in the flexibility of the polymer chain, which can

promote the migration of Li^+ . Similarly, the sample of PEO₁₈-LiTFSI electrolyte shows a T_m of 56.54°C , while the samples of MSEs exhibit lower values of T_m (56.19 to 41.92°C). This drop in T_m is consistent with decrease in bond density which is expected from higher disorder (reduced crystallinity), evidence of which is provided in the XRD data of Fig. 2a. According to the calculated results, χ_c decreases from 31.28% to 29.69% as LLZO is increased from 0 to 7.5% in the PEO₁₈-LiTFSI electrolyte. Furthermore, χ_c further decreases to 12.38% as the SN content increases from 0 to 10%. The results indicate that both inorganic LLZO particles and plastic crystal material SN can act to suppress polymer crystallization. Since the MSEs have lower crystallinity and higher amorphous phase fraction, their theoretical ionic conductivity should be much higher than that of PEO₁₈-LiTFSI electrolyte.

The effects of LLZO and SN contents on the ionic conductivities of MSEs were systematically investigated. Fig. 3a shows the Arrhenius plots with different compositions. As expected, the ionic conductivities increased significantly with increasing temperature for all the MSEs, owing to the faster movement of ions and polymer chains. The insert shows the variation of ionic conductivity with LLZO content at room temperature. It can be observed that the ionic conductivity of PEO₁₈-LiTFSI is only $2.92 \times 10^{-6} \text{ S} \cdot \text{cm}^{-1}$ at 25°C , while the electrolyte containing 7.5 wt% LLZO (PEO₁₈-LiTFSI-7.5%LLZO) possesses a much higher ionic conductivity of $1.19 \times 10^{-5} \text{ S} \cdot \text{cm}^{-1}$. However, further increase in the LLZO content may block conducting pathways of Li^+ and reduce the ionic conductivity, which may be due to the fact that more and more excessive LLZO particles block conducting pathways of Li^+ and further increase the crystallinity of the polymer.²⁹ Based on 7.5 wt% LLZO, adding a small amount of SN can further improve the ionic conductivity. MSE containing 10 wt% SN exhibits the maximum ionic conductivity of $1.19 \times 10^{-4} \text{ S} \cdot \text{cm}^{-1}$ at 25°C and $3.69 \times 10^{-4} \text{ S} \cdot \text{cm}^{-1}$ at 60°C . Therefore, the room-temperature ionic conductivity of PEO₁₈-LiTFSI-7.5%LLZO-10%SN electrolyte is ~ 40 -fold greater than that of PEO₁₈-LiTFSI. The increased ionic conductivities of PEO₁₈-LiTFSI-xLLZO-ySN electrolytes can be attributed to the following. SN particles can promote the dissolution of lithium salts, which increases the concentration of free charge carriers.¹³ Furthermore, SN reduces the crystallinity of the PEO phase as well as increases the proportion of the amorphous phase, which speeds up the movement of lithium ions.³⁵

As a vital component of the ASSLBs, solid electrolytes possessing wide electrochemical stability window can match higher operating voltage cathodes, which in turn increases the energy density of the ASSLBs. Therefore, the electrochemical stability has become a key factor in the development of high-energy-density ASSLBs. The potential windows of linear sweep voltammetry (LSV) traces are shown

Table I. Measured values of T_g , T_m , and ΔH_m and derived values of χ_c .

electrolytes	$T_g/^\circ\text{C}$	$T_m/^\circ\text{C}$	$\Delta H_m/\text{J} \cdot \text{g}^{-1}$	$\chi_c/\%$
PEO ₁₈ -LiTFSI	-48.21	56.54	63.50	31.28
PEO ₁₈ -LiTFSI-7.5%LLZO	-49.95	56.19	60.27	29.69
PEO ₁₈ -LiTFSI-7.5%LLZO-2.5%SN	-50.47	53.46	52.44	25.83
PEO ₁₈ -LiTFSI-7.5%LLZO-5%SN	-50.60	52.78	49.39	24.33
PEO ₁₈ -LiTFSI-7.5%LLZO-7.5%SN	-51.01	45.07	29.69	14.63
PEO ₁₈ -LiTFSI-7.5%LLZO-10%SN	-52.73	41.97	25.13	12.38

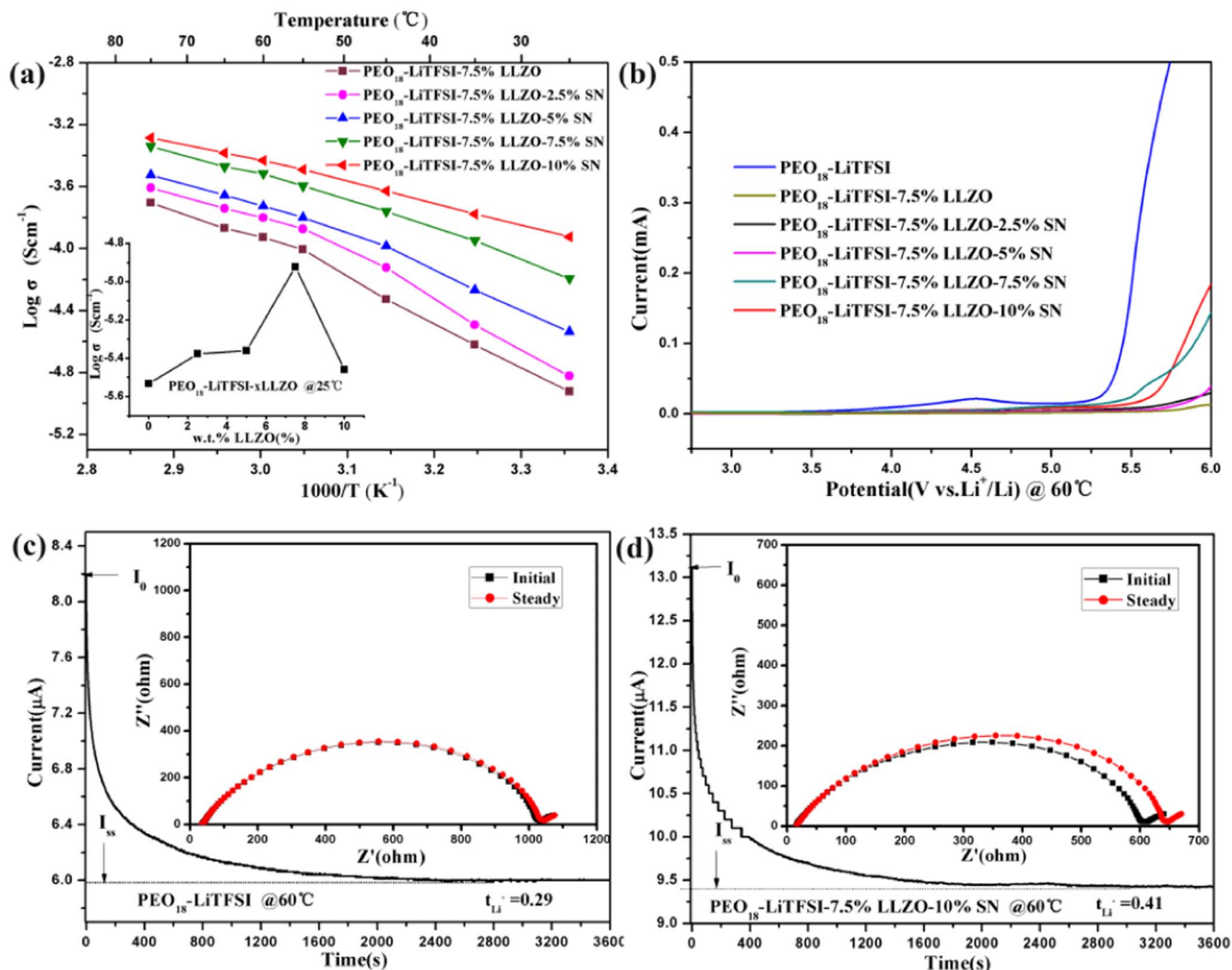


Figure 3. a) Variation of ionic conductivity of electrolyte with temperature and composition, b) linear sweep voltammetry curves at 60°C. DC polarization curve and the EISs before and after polarization for c) symmetric Li/PEO₁₈-LiTFSI/Li cell and d) symmetric Li/PEO₁₈-LiTFSI-7.5%LLZO-10%SN/Li cell.

in Fig. 3b. It is easy to see that the MSEs are electrochemically more stable than the PEO₁₈-LiTFSI electrolyte. For PEO₁₈-LiTFSI there is a small anodic peak near the potential of 4.5 V vs. Li/Li⁺, corresponding to the oxidative decomposition of PEO. Another peak subsequently occurs around 5.2 V vs. Li/Li⁺, corresponding to the oxidative decomposition of polymer and lithium salt.¹⁹ Nevertheless, the PEO₁₈-LiTFSI-7.5%LLZO-10%SN possesses enhanced oxidative stability of 5.5 V vs. Li/Li⁺. This makes this innovative electrolyte with a wide electrochemical stability window an attractive promising electrolyte for high-energy-density ASSLBs. The broadened electrochemical stability window may be attributed to the effect of LLZO fillers. It is well known that LLZO has a wide electrochemical window. Furthermore, salt anions TFSI⁻ tends to bond with the acidic surface sites of LLZO, which inhibits the mobility of the anions through a sort of 'Lewis acid-base' interaction or 'ion-ceramic complex' formation.³⁶ Hence, the irreversible oxidation reaction between

anions (TFSI⁻) and electrolyte will reduce, which is beneficial for the improvement of oxidative stability.³⁷ This result is consistent with t_{Li^+} as shown in Table II. The values for PEO₁₈-LiTFSI-7.5%LLZO (Fig. S2) and PEO₁₈-LiTFSI-7.5%LLZO-10%SN (Fig. 3d) are much higher than that of PEO₁₈-LiTFSI (Fig. 3c). This can be explained by the fact that LLZO particles can greatly limit the movement of anions. Moreover, SN particles can increase the concentration of Li⁺ by promoting the dissolution of the lithium salt, which may attribute to the significant improvement of t_{Li^+} .^{13,36} This high t_{Li^+} not only indicates an excellent Li⁺-dominant conduction behavior but also can be expected to reduce polarization and raise the rate performance of ASSLBs during charge and discharge process.

For high-energy-density lithium batteries, the interfacial compatibility of solid electrolytes against lithium metal is critical to the ASSLB's cycling life and performance. Fig. 4a shows the evolution of the interfacial resistance (R_i) over time for Li symmetric cells

Table II. The values of I_0 , I_{ss} , R_0 , R_{ss} , and the calculated values of t_{Li^+} at 60°C.

electrolytes	$I_0/\mu A$	$I_{ss}/\mu A$	R_0/Ω	R_{ss}/Ω	$\Delta V/mV$	t_{Li^+}
PEO ₁₈ -LiTFSI	8.20	5.997	1035	1043	10	0.29
PEO ₁₈ -LiTFSI-7.5%LLZO	12.37	9.663	670	680	10	0.39
PEO ₁₈ -LiTFSI-7.5%LLZO-10%SN	13.05	9.421	586	626	10	0.41

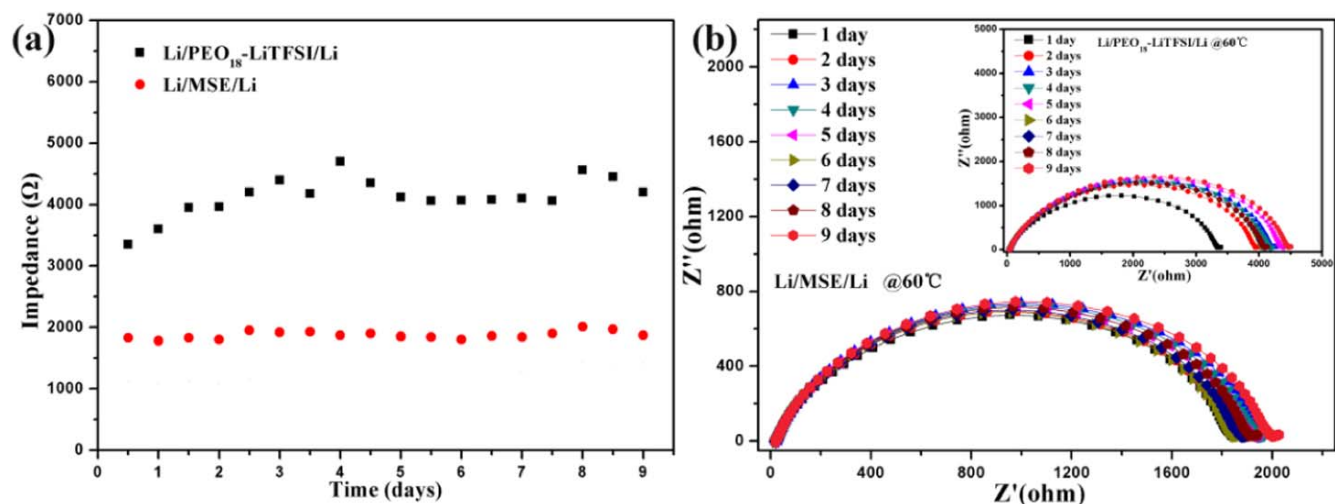


Figure 4. a) The evolution of the interfacial resistance (R_i) for Li symmetric cells after various storage times at 60°C, b) EIS for Li/MSE/Li and $\text{Li/PEO}_{18}\text{-LiTFSI/Li}$ symmetric cells.

fitted with $\text{PEO}_{18}\text{-LiTFSI}$ electrolyte and $\text{PEO}_{18}\text{-LiTFSI-7.5\%LLZO-10\%SN}$ electrolyte. It can be seen that the interfacial stability of MSE against lithium is much greater than that of $\text{PEO}_{18}\text{-LiTFSI}$. From the AC impedance spectra shown in Fig. 4b the values of overall R_i for $\text{PEO}_{18}\text{-LiTFSI}$ rose continuously during 9 days (from 3350 Ω to 4200 Ω), while the values of overall R_i for MSE remain stable after a small increase (from 1830 Ω to 1870 Ω). However, the overall R_i for MSE is much smaller than that of $\text{PEO}_{18}\text{-LiTFSI}$ suggesting excellent interfacial contact and compatibility with the lithium electrode. The improvement in interfacial contact may be due to the plasticization effect of SN.³²

Application of MSE as a scalable solid electrolyte for ASSLBs.—

Finally, ASSLBs with the MSE ($\text{PEO}_{18}\text{-LiTFSI-7.5\%LLZO-10\%SN}$) were fitted. The schematic illustration of the synthesis of the MSE-based ASSLBs is shown in Fig. 5. The cycling and rate performances of ASSLBs ($\text{LiFePO}_4/\text{Li}$) were systematically studied. The

initial cycling curves at different current rates at 60°C are shown in Fig. 6a. The initial discharge specific capacities of the MSE-based batteries at 0.2 C, 0.5 C, 1 C, and 2 C are 157.9, 145.6, 130.2, and 122.1 $\text{mAh}\cdot\text{g}^{-1}$, respectively. Relatively speaking, the cell exhibits a low voltage polarization. When operated at 0.2 C, the voltage plateaus for charge and discharge process are around 3.47 and 3.38 V. The low polarization voltage of the cells is attributed to the improved ionic conductivity and the improved interfacial contact between electrolyte and electrodes.³⁸ The impedance spectra of Li/MSE/LiFePO_4 and $\text{Li/PEO}_{18}\text{-LiTFSI/LiFePO}_4$ cells are shown in Fig. S3. It is evident that the interfacial resistance of the MSE-based cell ($\sim 130\ \Omega$) is much smaller than that of the $\text{PEO}_{18}\text{-LiTFSI}$ cell ($\sim 300\ \Omega$) due to the improved interfacial contact.

Fig. 6b presents the rate performance of the MSE-based cell from 0.2 C to 2 C at 60°C. The discharge capacity of the cell monotonically decreases with increasing current density due to polarization.

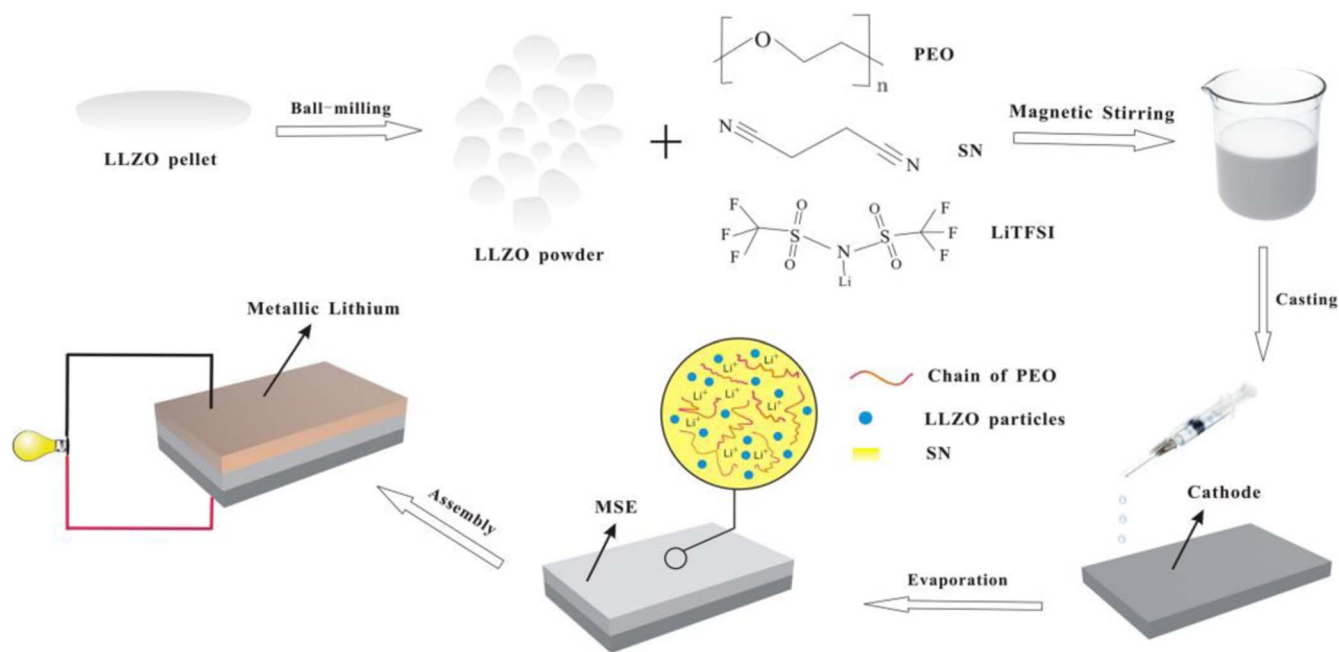


Figure 5. Schematic illustration of synthesis of the MSE-based batteries.

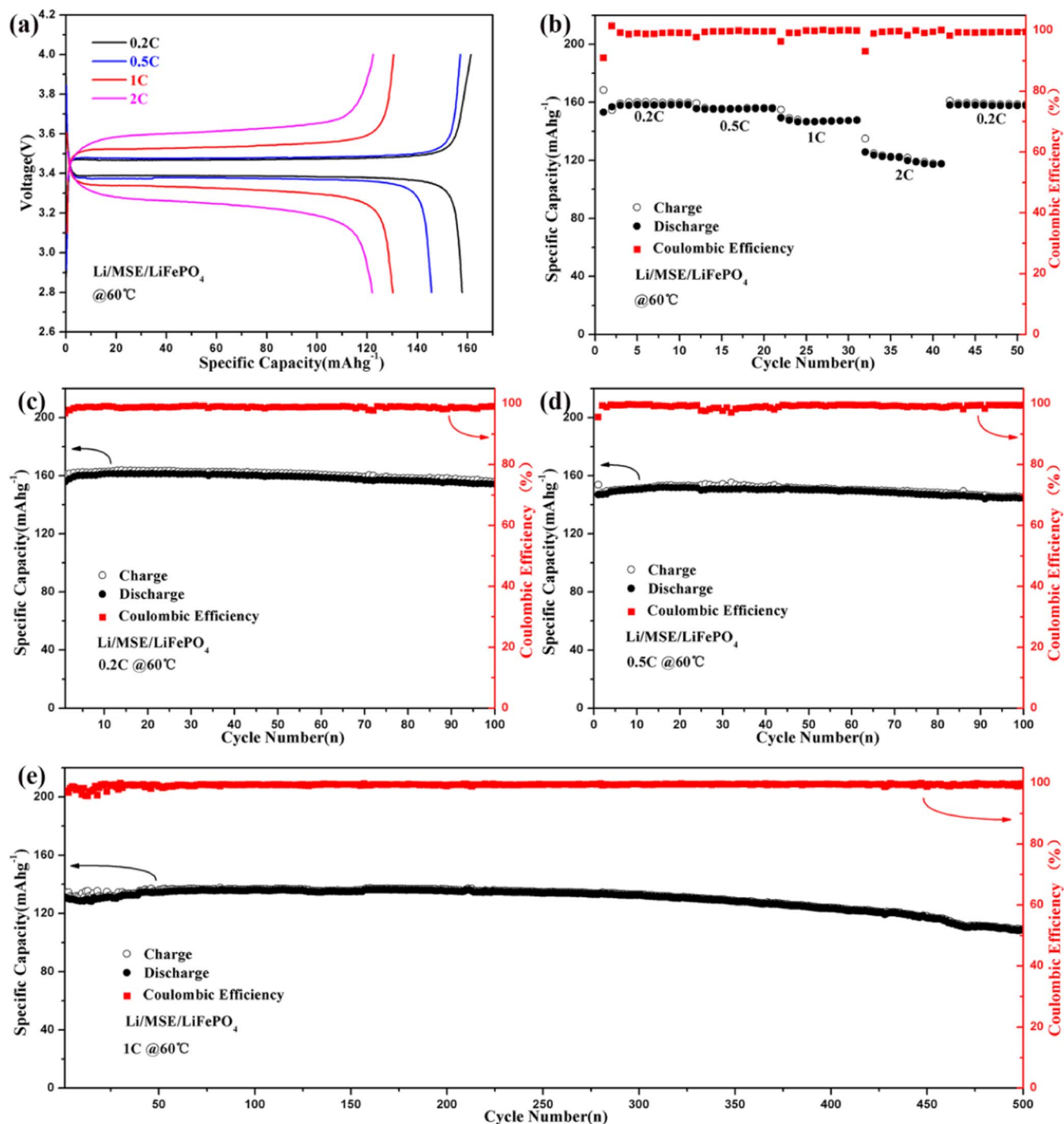


Figure 6. Cycling and rate performance of ASSLBs at 60°C: a) the initial cycling curves at different rates, b) the rate performance of the cell from 0.2 C to 2 C, the cycling performance c) at 0.2 C, d) at 0.5 C, and e) at 1 C.

When operating at high current density of 2 C, the cell still delivers a relatively high specific capacity ($\sim 120 \text{ mAh} \cdot \text{g}^{-1}$). In addition, the capacity can be quickly restored to $160 \text{ mAh} \cdot \text{g}^{-1}$ when the current density returns to 0.2 C. This result proves that MSE-based ASSLBs can be safely operated over a wide range of current density without incurring damage.

The cycling performances of the MSE-based batteries at 0.2 C, 0.5 C and 1 C are illustrated in Fig. 6c, Fig. 6d and Fig. 6e, respectively. As shown in Fig. 6c, the maximum discharge specific capacity of the cell is $161.2 \text{ mAh} \cdot \text{g}^{-1}$. After 100 cycles, the specific discharge capacity is $154.2 \text{ mAh} \cdot \text{g}^{-1}$, which is 95.7% of the maximum value.

When the cell was operated at 0.5 C, it exhibits a maximum discharge specific capacity of $152 \text{ mAh} \cdot \text{g}^{-1}$ after the first few cycles. Subsequently, the capacity dropped slightly to $144.7 \text{ mAh} \cdot \text{g}^{-1}$ after 100 cycles, corresponding to a capacity retention rate of 95.2%. This result indicates the excellent cycling performance of MSE-based ASSLBs. Fig. S4 shows the EIS of the MSE-based cell before charging and after 100 cycles at 0.5 C. The negligible change in interfacial resistance suggests that the interface between electrodes and electrolyte remains stable during the process of cycling,¹⁴ which attributes to the superior cycling performance of the Li/MSE/LiFePO₄ cell as shown in Fig. 6c and Fig. 6d.

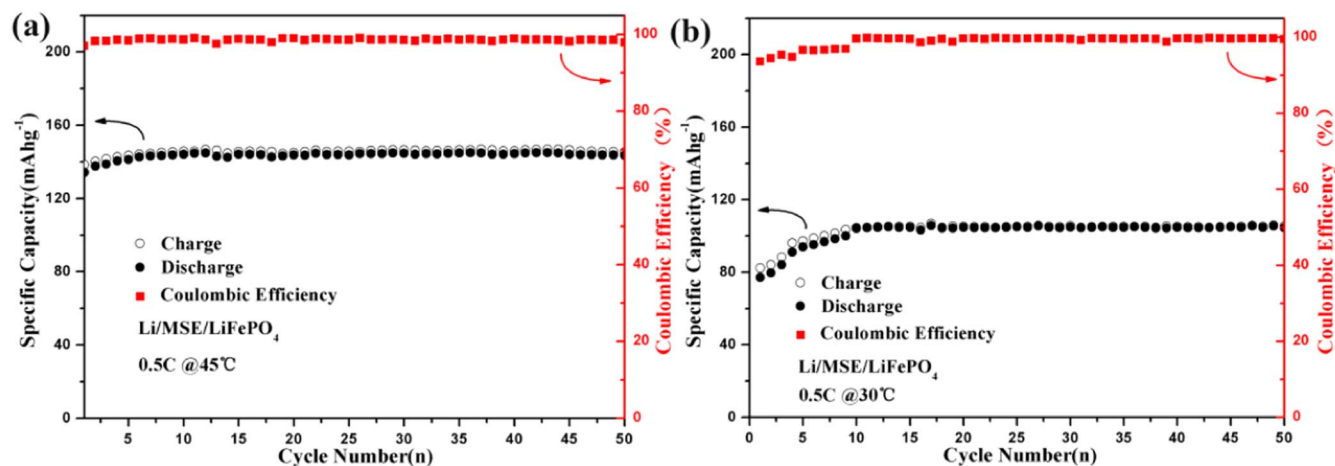


Figure 7. The cycling performance of the Li/PEO₁₈-LiTFSI-7.5%LLZO-10%SN/LiFePO₄ batteries at different temperatures: a) 45°C and b) 30°C.

In an effort to attain a more comprehensive understanding of the cycling performance at high current density, the ASSLBs were also tested at 1 C and 2 C. As depicted in Fig. 6e, the MSE-based cell exhibits excellent cycling stability at 1 C. After initial activation, the discharge specific capacity stabilized at around 135 mAh·g⁻¹ and slightly decreased after 250 cycles. The specific capacities of the 100th, 200th, 300th, 400th and 500th cycle are 136.0, 135.1, 132.5, 123.3 and 108.8 mAh·g⁻¹, respectively. Capacity retention rate is 80.0% after 500 cycles, and the coulombic efficiency of the cell is in the range of 99.3~99.7%. Moreover, the cell still provides a relatively high specific capacity of 111.6 mAh·g⁻¹ after 50 cycles (Fig. S5). We have assembled ASSLB with LiCoO₂ as the cathode material and tested its cell performance, which is displayed in Fig. S6. The cycling performance of the Li/MSE/LiCoO₂ battery at 0.2 C and 60°C shows that the maximum discharge specific capacity of the cell is 136 mAh·g⁻¹. After 50 cycles, the specific discharge capacity is 131 mAh·g⁻¹.

The cycling performance of MSE-based batteries was measured at lower temperatures, results reported in Fig. 7. Before running at different temperatures, these batteries were kept at 60°C for two hours. A pre-heat-treatment process can effectively shorten the activation process since the softened electrolyte membrane enjoys improved interface contact.²⁶ The specific capacities of the cells operating at 45°C and 30°C show significant decrease compared to the cell operating at 60°C in Fig. 6d. Even so, it is worth noting that the cell operating at 30°C still displays a discharge capacity of 104.2 mAh·g⁻¹ after 50 cycles at 0.5 C. In other words, the low temperature cycling performance of the Li/MSE/LiFePO₄ cell is acceptable, even superior to that of many reported studies of ASSLBs,^{22,38,39} yet deserving of further improvements in the low-temperature ionic conductivity of the solid electrolyte.

Conclusions

A scalable multifunctional solid electrolyte (MSE) for ASSLBs was prepared by conventional solution-casting technique. Notably, this MSE showed a maximum conductivity of 1.19×10^{-4} S·cm⁻¹ at ambient temperature, and the potential window rose to 5.5 (V vs. Li⁺/Li). Moreover, the Li⁺ transference number of this MSE has been greatly improved, indicating an excellent Li⁺-dominant conduction behavior. Finally, the MSE (PEO₁₈-LiTFSI-7.5%LLZO-10%SN) was fitted into ASSLBs, and the LiFePO₄/Li batteries exhibited outstanding cycling and rate performance. When these batteries were run under 60°C, the initial discharge specific capacities at 0.2 C, 0.5 C, 1C, and 2 C were 157.9, 145.6, 130.2, and 122.1 mAh·g⁻¹, respectively. The 500th discharge specific capacity of this cell operating at 1 C is 108.8 mAh·g⁻¹, and 80.0% of the capacity can be retained. We believe that such scalable multifunctional solid electrolytes with

enhanced performance can be put forth as promising candidates for next-generation electrolytes to replace conventional flammable liquid electrolytes and separator membranes for ASSLBs.

Acknowledgments

This work is financially supported by the National Key Research and Development Program of China (No. 2018YFB0905600, 2017YFB0310400), the National Natural Science Foundation of China (No. 51472188, and 51521001), Fundamental Research Funds for the Central Universities in China, State Key Laboratory of Advanced Electromagnetic Engineering and Technology (Huazhong University of Science and Technology), and the “111” project (No. B13035).

ORCID

Fei Chen <https://orcid.org/0000-0001-9643-7191>

Donald R. Sadoway <https://orcid.org/0000-0003-1978-8654>

References

- P. G. Bruce, S. A. Freunberger, L. J. Hardwick, and J. M. Tarascon, *Nature Mater.*, **11** (2012).
- B. Dunn and J. M. Tarascon, *Science*, **334**, 928 (2011).
- C. Deviannapoorani, L. Dhivya, S. Ramakumar, and R. Murugan, *J. Sol-Gel Sci. Technol.*, **64**, 510 (2012).
- C. L. Tsai, V. Roddatis, C. V. Chandran, Q. Ma, S. Uhlenbruck, M. Bram, P. Heitjans, and O. Guillon, *ACS Appl. Mater. Interfaces*, **8**, 10617 (2016).
- K. N. H. K. Y. Y. H. M. K. R. Y. M. K. T. K. Y. H. S. K. K. and M. A., *Nature Mater.*, **10**, 682 (2011).
- R. Prasanth, V. Aravindan, and M. Srinivasan, *J. Power Sources*, **202**, 299 (2012).
- K. H. Choi, S. J. Cho, S. H. Kim, Y. H. Kwon, J. Y. Kim, and S. Y. Lee, *Adv. Funct. Mater.*, **24**, 44 (2014).
- W. Liu, N. Liu, J. Sun, P. C. Hsu, Y. Li, H. W. Lee, and Y. Cui, *Nano Lett.*, **15**, 2740 (2015).
- Y. L. Ni'Mah, M. Y. Cheng, J. H. Cheng, J. Rick, and B. J. Hwang, *J. Power Sources*, **278**, 375 (2015).
- J. G. Kim, B. Son, S. Mukherjee, N. Schuppert, A. Bates, O. Kwon, M. J. Choi, H. Y. Chung, and S. Park, *J. Power Sources*, **282**, 299 (2015).
- S. Srivastava, J. L. Schaefer, Z. Yang, Z. Tu, and L. A. Archer, *Adv. Mater.*, **26**, 201 (2014).
- P. P. Soo, B. Huang, Y. I. Jang, Y. M. Chiang, D. R. Sadoway, and A. M. Mayes, *J. Electrochem. Soc.*, **146**, 32 (1999).
- L. Z. Fan, Y. S. Hu, A. J. Bhattacharyya, and J. Maier, *Adv. Funct. Mater.*, **17**, 2800 (2010).
- D. Zhou, Y. B. He, R. Liu, M. Liu, H. Du, B. Li, Q. Cai, Q. H. Yang, and F. Kang, *Adv. Energy Mater.*, **5** (2015).
- N. Pyllylän, M. Letiche, M. K. S. Barr, and T. Djenizian, *Electrochem. Commun.*, **43**, 121 (2014).
- K. Liu, F. Ding, J. Liu, Q. Zhang, X. Liu, J. Zhang, and Q. Xu, *ACS Appl. Mater. Interfaces*, **8** (2016).
- W. Wang, E. Yi, A. J. Fici, R. M. Laine, and J. Kieffer, *J. Phys. Chem. C*, **121**, 2563 (2017).

18. Y. Zhao, C. Wu, G. Peng, X. Chen, X. Yao, Y. Bai, F. Wu, S. Chen, and X. Xu, *J. Power Sources*, **301**, 47 (2016).
19. Y. Zhao, Z. Huang, S. Chen, B. Chen, J. Yang, Q. Zhang, F. Ding, Y. Chen, and X. Xu, *Solid State Ionics*, **295**, 65 (2016).
20. J. H. Choi, C. H. Lee, J. H. Yu, C. H. Doh, and S. M. Lee, *J. Power Sources*, **274**, 458 (2015).
21. F. Langer, I. Bardenhagen, J. Glenneberg, and R. Kun, *Solid State Ionics*, **291**, 8 (2016).
22. Y. C. Jung, M. S. Park, C. H. Doh, and D. W. Kim, *Electrochim. Acta*, **218**, 271 (2016).
23. R. Murugan, V. Thangadurai, and W. Weppner, *Angew. Chem.*, **46**, 7778 (2007).
24. J. C. Bachman, S. Muy, A. Grimaud, H. H. Chang, N. Pour, S. F. Lux, O. Paschos, F. Maglia, S. Lupart, and P. Lamp, *Cheminform*, **116**, 140 (2016).
25. J. F. Wu, K. P. Wei, V. K. Peterson, W. Lu, and G. Xin, *ACS Appl. Mater. Interfaces*, **9**, 12461 (2017).
26. R. Chen, Y. Zhang, T. Liu, B. Xu, Y. H. Lin, C. Nan, and Y. Shen, *ACS Appl. Mater. Interfaces*, 9654 (2017).
27. K. Fu, Y. Gong, G. T. Hitz, D. W. McOwen, Y. Li, S. Xu, Y. Wen, L. Zhang, C. Wang, G. Pastel, J. Dai, B. Liu, H. Xie, Y. Yao, E. D. Wachsman, and L. Hu, *Energy Environ. Sci.*, **10**, 1568 (2017).
28. S. H. Kim, K. H. Choi, S. J. Cho, J. S. Park, K. Cho, C. Lee, S. Lee, J. Shim, and S. Y. Lee, *J. Mater. Chem. A*, **2**, 10854 (2014).
29. F. Chen, D. Yang, W. Zha, B. Zhu, Y. Zhang, J. Li, Y. Gu, Q. Shen, L. Zhang, and D. R. Sadoway, *Electrochim. Acta*, **258**, 1106 (2017).
30. Y. Zhang, F. Chen, R. Tu, Q. Shen, L. Zhang, and J. Power Sources, **268**, 960 (2014).
31. M. R. Johan, O. H. Shy, S. Ibrahim, S. M. M. Yassin, and T. Y. Hui, *Solid State Ionics*, **196**, 41 (2011).
32. W. Zha, F. Chen, D. Yang, Q. Shen, L. Zhang, and J. Power Sources, **397**, 87 (2018).
33. X. L. Wu, S. Xin, H. H. Seo, J. Kim, Y. G. Guo, and J. S. Lee, *Solid State Ionics*, **186**, 1 (2011).
34. L. Hu, Z. Tang, and Z. Zhang, *J. Power Sources*, **166**, 226 (2007).
35. S. Cheng, D. M. Smith, and C. Y. Li, *Macromolecules*, **43**, 3978 (2014).
36. F. Croce, L. Persi, B. Scrosati, F. Serraino-Fiory, E. Plichta, and M. A. Hendrickson, *Electrochim. Acta*, **46**, 2457 (2002).
37. J. Zhou and P. S. Fedkiw, *Solid State Ionics*, **166**, 275 (2004).
38. B. Chen, Z. Huang, X. Chen, Y. Zhao, Q. Xu, P. Long, S. Chen, and X. Xu, *Electrochim. Acta*, **210**, 905 (2016).
39. J. Zhang, N. Zhao, M. Zhang, Y. Li, P. K. Chu, X. Guo, Z. Di, X. Wang, and H. Li, *Nano Energy*, **28**, 447 (2016).